First hydrothermal discoveries on the Australian-Antarctic Ridge: Discharge sites, plume chemistry, and vent organisms

Doshik Hahm[1,6], Edward T. Baker[2], Tae Siek Rhee[1], Yong-Jin Won[3], Joseph A. Resing[2], John E. Lupton[4], Won-Kyung Lee[5], Minjeong Kim[6], and Sung-Hyun Park[1]

[1]Korea Polar Research Institute, Incheon, Republic of Korea, [2]Joint Institute for the Study of the Atmosphere and Ocean, University of Washington, and NOAA-PMEL, Seattle, Washington, USA, [3]Department of Life Science, Ewha Womans University, Seoul, Republic of Korea, [4]NOAA/PMEL, Newport, Oregon, USA, [5]Division of EcoScience, Ewha Womans University, Seoul, Republic of Korea, [6]Department of Polar Sciences, Korea University of Science and Technology, Incheon, Republic of Korea

Abstract The Australian-Antarctic Ridge (AAR) is one of the largest unexplored regions of the global mid-ocean ridge system. Here, we report a multiyear effort to locate and characterize hydrothermal activity on two first-order segments of the AAR: KR1 and KR2. To locate vent sites on each segment, we used profiles collected by Miniature Autonomous Plume Recorders on rock corers during R/V *Araon* cruises in March and December of 2011. Optical and oxidation-reduction-potential anomalies indicate multiple active sites on both segments. Seven profiles on KR2 found 3 sites, each separated by ~25 km. Forty profiles on KR1 identified 17 sites, some within a few kilometer of each other. The spatial density of hydrothermal activity along KR1 and KR2 (plume incidence of 0.34) is consistent with the global trend for a spreading rate of ~70 mm/yr. The densest area of hydrothermal activity, named "Mujin," occurred along the 20 km-long inflated section near the segment center of KR1. Continuous plume surveys conducted in January–February of 2013 on R/V *Araon* found $CH_4/^3He$ ($1 - 15 \times 10^6$) and CH_4/Mn (0.01–0.5) ratios in the plume samples, consistent with a basaltic-hosted system and typical of ridges with intermediate spreading rates. Additionally, some of the plume samples exhibited slightly higher ratios of $H_2/^3He$ and Fe/Mn than others, suggesting that those plumes are supported by a younger hydrothermal system that may have experienced a recent eruption. The Mujin-field was populated by *Kiwa* crabs and seven-armed *Paulasterias* starfish previously recorded on the East Scotia Ridge, raising the possibility of circum-Antarctic biogeographic connections of vent fauna.

1. Introduction

Hydrothermal vents on the mid-ocean ridge (MOR) system strongly affect ocean chemistry and provide energy sources for biological communities in the deep sea [e.g., *Corliss et al.*, 1979; *Van Dover*, 2000; *German and Seyfried*, 2014]. More than 400 vent sites have now been identified on MORs throughout the global ocean, but these discoveries have been strongly biased to low-latitude ridges [*Beaulieu et al.*, 2013]. Extreme weather and remoteness from capable ports have deterred exploration in the high-latitude ridges of southern oceans. Circum-Antarctic Ridges (CAR), which encircle Antarctica and extend around the southern hemisphere for ~21,000 km, constitute one third of global ridge system but presently account for only ~10% of known sites. The InterRidge vents database (http://vents-data.interridge.org) lists 38 locations inferred from plume measurements on CAR [*Beaulieu et al.*, 2013], but only two on the East Pacific Rise (EPR) near 37.7°S [*Stoffers et al.*, 2002] and one on the Southwest Indian Ridge (SWIR) at 49.65°E [*Tao et al.*, 2007] have been confirmed by seafloor visualization.

The Australian-Antarctic Ridge (AAR), located in the northwest of the Ross Sea at Antarctica, is the largest unexplored expanse of CAR (Figure 1). In the austral summers of 2011 and 2013, the Korea Polar Research Institute (KOPRI) conducted three surveys (KORRIDGE Legs 1-3) of two segments at 160°E (KR1) and 152.5°E (KR2) using the icebreaker R/V *Araon* (Figure 1). We found strong evidence of hydrothermal venting on both segments using MAPRs (Miniature Autonomous Plume Recorder, e.g., *Baker et al.* [2010]), CTD tow-yos, and chemical analyses of water samples collected in Niskin bottles on CTD/Rosette. Multiple active sites in the
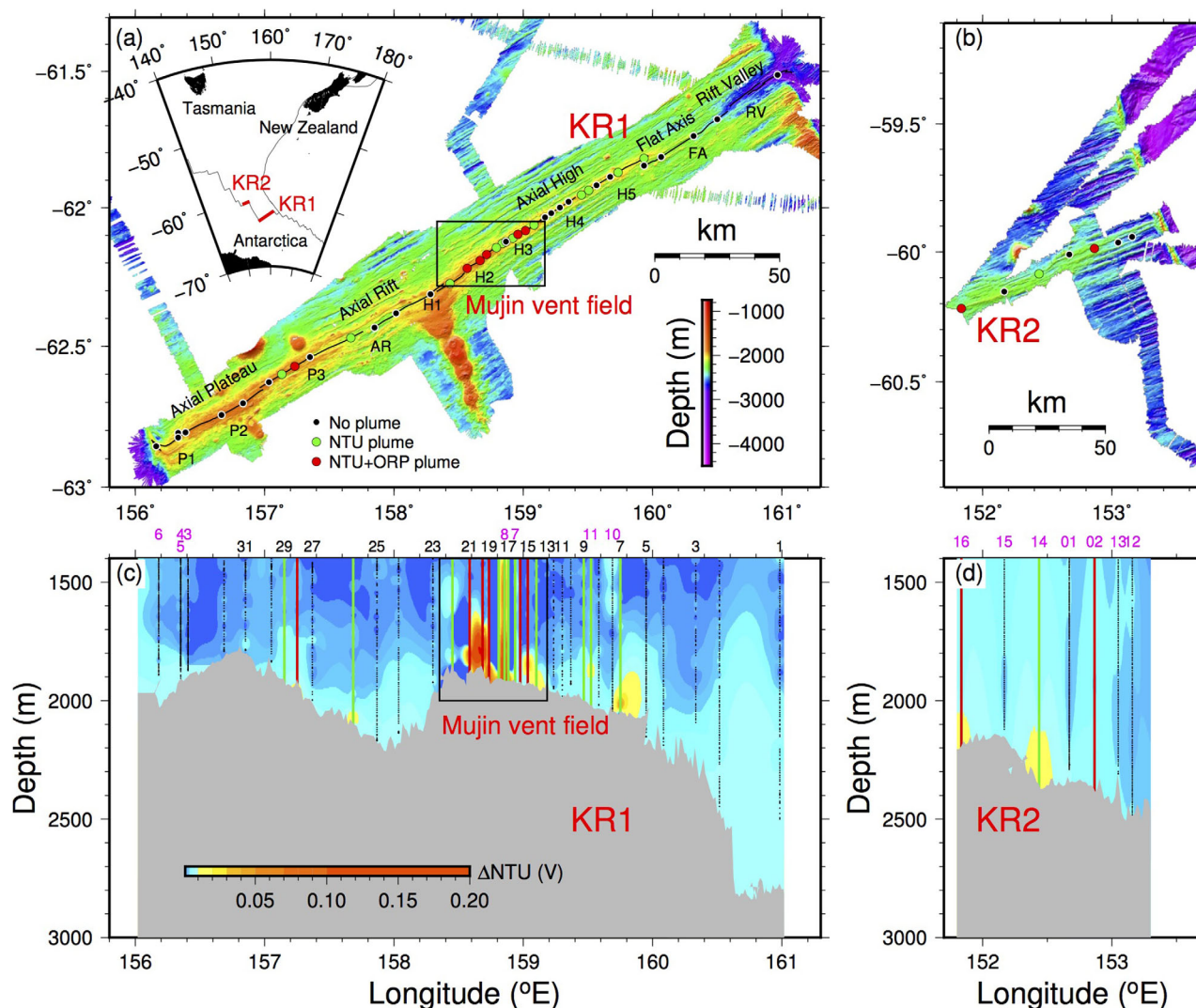
Figure 1. Bathymetry of KR1 (a) and KR2 (b). Eleven identified segments and five areas on KR1 are labeled along the ridge. The colored circles on the bathymetric maps indicate the locations of MAPR profiles and the characteristics of the plumes (see the legend in Figure 1a for color code). The inset in Figure 1a shows the location of KR1 and KR2. ΔNTU contour plots of KR1 and KR2 are shown in Figures 1c and 1d, respectively. The magenta and black numbers above the contour plots indicate station numbers in March and December 2011 (only the odd-numbered December stations are labeled), respectively. Mujin vent field is designated in black rectangle in Figures 1a and 1c.

middle of the 300 km-long supersegment KR1 make up the "Mujin (Misty Harbor)" vent field (Figure 1). During Leg 3, we recovered vent organisms from the Mujin vent field during dredges for rock collection. In this paper, we report the distribution and chemistry of hydrothermal plumes on KR1 and KR2, and provide brief descriptions of the vent organisms. Geochemical data for the rock samples obtained during the cruises will be published in separate papers.

Active vents discovered in this region are more geographically isolated from confirmed hydrothermal sites than any others. To the west, sites on the Southeast Indian Ridge near 100°E are 4300 km distant. To the east, the nearest confirmed hydrothermal plumes lie 6400 km away on the Pacific-Antarctic Ridge (PAR) at 38°S [Beaulieu et al., 2013]. Therefore the discovery and chemical characterization of hydrothermal vents on the AAR would be an important step for evaluating hydrothermal activity in the southern ocean. Furthermore, prior to these expeditions, there was no information on biogeographical provinces along some 15,000 km from the Rodrigues Triple Junction in the central Indian Ocean to around 38°S below the Easter Microplate in the Pacific Ocean [Van Dover et al., 2002]. Our recovery of vent organisms from the AAR provides further insights into patterns of global vent biogeography.

2. Geological Setting

The AAR is a series of ridge segments and transform faults extending from 140°E to 180° (Figure 1a inset). The spreading rate is intermediate ($\sim$70 mm/yr) and its axial depth is relatively shallow ($\sim$2200 m) [*Choi et al.*, 2013]. The KR1 and KR2 first-order segments bounded by transform faults are the most southerly AAR segments (Figures 1a and b). Bathymetric maps for the two segments were made based on multibeam echosounder (Kongsberg EM122) data from all three cruises.

The 300 km-long supersegment KR1 is the longest on CAR between 139.5°E and 122°W. KR1 shows large variations in its axial morphology and contains five distinct areas from west to east: an axial high plateau (P1–P3), a small axial rift valley (AR), a narrow axial high with a small graben (H1–H5), a flat region with no high or valley (FA), and a pronounced axial valley (RV) (Figure 1a). This variability in axial morphology suggests that magma supply has varied on short spatial scales within KR1. An off-axis seamount chain intersects the ridge at 158.33°E, where the ridge morphology changes from axial rift to axial high. Although the axial depth is $\sim$2000 m along most of the ridge, the eastern end deepens sharply to $\sim$2900 m inside an axial valley $\sim$700 m deep. The five morphological areas can be subdivided into 11 segments based on small-scale axial discontinuities ($<$4 km) (Figure 1a). KR1 has no offsets larger than 4 km along its entirety.

KR2 is a 180 km-long segment that steadily deepens from 2200 m in the west to 2500 m in the east. An offset at 152.30°E divides KR2 into two segments, an eastern rift valley and a western axial high (Figure 1b). The variability of the magma supply is apparently lower than at KR1.

3. Methods

3.1. Hydrothermal Plume Detection and Sampling

Our hydrothermal survey of KR1 and KR2 began with eight stations on KR1 and seven on KR2 in March 2011, followed by 32 stations on KR1 in December 2011 (Figure 1). At each station, we attached MAPRs 20 and 40 m above the rock core [*Reynolds et al.*, 1992]. At two stations, a MAPR was attached to a SBE 911plus Conductivity-Temperature-Depth (CTD) package. MAPRs recorded pressure, temperature, light backscattering, and oxidation-reduction potential (OPR, sometimes referred to as Eh) every 5 s, or about every 5–8 m depth interval. Light backscattering is reported as nephelometric turbidity units [NTU; *American Public Health Association*, 1985]; ΔNTU is the value above ambient, nonplume water. The ORP sensor measures the potential, E (mV), between a Pt electrode in seawater and an Ag-AgCl reference electrode in a saturated KCl solution. Lower voltages relative to ambient water are indicative of reduced hydrothermal species, including HS^- and Fe^{2+}, which are out of equilibrium with the oxidizing ocean. Its response is roughly inversely proportional to plume "age" as these species are oxidized, metabolized, and diluted while mixing with ambient seawater. Previous field experience [e.g., *German et al.*, 2008; *Baker et al.*, 2010], tows across the axis of KR1 (see section 4.2), and laboratory studies [*Walker et al.*, 2007] indicate that detectable ORP anomalies are degraded quickly and are rarely found farther than $\sim$1 km from their seafloor source. Absolute values of E can vary because of instrumental drift and hysteresis (the response is instantaneous but recovery time can last several to tens of minutes), especially in concentrated plumes, so we rely on the time derivative, dE/dt (mV/s) to identify the precise location of anomalies. Because E declines when it encounters reduced substances, the anomalies are negative.

In February 2013, we exclusively used the CTD with integrated light backscattering and ORP sensors to conduct 12 vertical casts and five tow-yos (CTDs 02, 14, 16, 17, and 18 in Figure 3) on and around KR1. For tows, the CTD package was continuously raised and lowered through a vertical range of $\sim$200 m as the R/V *Araon* transited at $\sim$3–4 km/h. Each vertical profile was inspected for prominent density inversions accompanied by the presence of a dE/dt anomaly. This combination indicated that the CTD had passed through a rising hydrothermal plume and was close to a vent. Altitudes above seafloor were obtained using an altimeter attached to the bottom of the CTD/rosette frame.

3.2. Analyses of Plume Samples

To investigate the distribution of chemical species in the hydrothermal plumes, samples were collected in February 2013 using Niskin bottles mounted on CTD/Rosette. Aliquots of seawater were drawn from the Niskin bottles in the order of helium, other dissolved gases (H_2 and CH_4), and metals (Fe and Mn). Water samples for helium isotopes were collected in fresh copper tubes using the cold crimping method

described by *Young and Lupton* [1983]. Helium isotopes were analyzed on a dual-collector noble gas mass spectrometer at the Helium Isotope Laboratory, NOAA/PMEL, Newport, Oregon, USA. The 1-σ uncertainty in the ^{3}He/^{4}He ratio is about 0.2%. The details of ^{3}He/^{4}He measurement are found in *Lupton* [1990] and *Lupton and Evans* [2013].

Seawater samples for dissolved gases were drawn into specially designed glass containers. In the laboratory, a precisely known volume of pure N_2 (99.9999%) was injected into the glass containers to make headspace. After equilibration with dissolved gases, the headspace air was taken using a gas tight syringe (SGE Analytical Science) and injected into sample loops equipped in the gas chromatographs. CH_4 was separated in a packed column (Porapak Q 50/80, Restek), detected by flame ionization detector (FID), and quantified by calibrating the gas chromatographic system using a series of calibration gases [*Rhee et al.*, 2009]. H_2 was separated in a molecular sieve packed column and detected by Hg vapor which was proportionally produced by the reaction of H_2 with HgO in a hot bed at 250°C (RGA3, Trace Analytical) [*Rhee*, 2000]. Gas chromatography for H_2 measurements was calibrated using a series of calibration gases scaled to World Meteorological Organization's (WMO) Global Atmospheric Watch (GAW) H_2 mole fraction [*Jordan and Steinberg*, 2011].

Unfiltered samples for total dissolvable Mn and Fe (TDMn and TDFe) were collected directly from the Niskin sampling bottles into 125 mL I-Chem polyethylene bottles. The metals samples were then acidified with 0.5 mL of subboiling quartz distilled 6N HCl. Mn was determined with a precision of 1 nM by modifying the direct injection method of *Resing and Mottl* [1992] by adding 4 g of nitrilotriacetic acid to each liter of buffer. Fe was determined with a precision of ± 2 nM by modifying the method of *Measures et al.* [1995] for direct injection analysis.

We regard CTD01 and CTD13 as background stations because they did not display NTU or ORP anomalies at depth and had no significant enrichments in chemical tracers of hydrothermal activity. CTD01 was located 45 km away from KR1 and thus was not expected to observe any hydrothermal signals. The background values of ^{3}He (2.85 $\pm$ 0.04 fmol/kg), CH_4 (0.62 $\pm$ 0.23 nmol/kg), and H_2 (0.14 $\pm$ 0.09 nmol/kg) were determined as the mean and standard deviation of the observed values between 1600 and 1900 m depths of the background stations. For the purposes of this study, background Mn and Fe are assigned values of zeros because many of the water samples did not exceed the 1 nM detection limit of the methods used to determine Fe and Mn. The background values were subtracted from measured values to derive elemental ratios in section 5.2.

3.3. Collection and Molecular Identification of Vent Organisms

Vent-associated animals were caught by chance during our dredging survey of rock samples within Mujin vent field in 2013 (Figures 1a and 1c). The icebreaker R/V *Araon* pulled a heavy dredge fitted with a tight net for 200–500 m along transects designed to cross-targeted spots for rock samples. Upon recovery of the dredging equipment on shipboard, the net was routinely examined for bycatch. Nine individuals of yeti crabs and a seven-armed starfish were caught and then preserved in 95% ethanol prior to taxonomic and DNA examination on land. For molecular identification of the yeti crabs, mitochondrial 16S rRNA gene was amplified and sequenced from two individuals as described by *Rogers et al.* [2012]. The obtained sequences (GenBank accession KP743035-KP743036) of the two yeti crabs were analyzed and compared with previously published data of all the known *Kiwa* species from other vents and seep using the computer program, MEGA v. 6.0.5 [*Tamura et al.*, 2013]. For identification of the seven-armed starfish, mitochondrial 16S rRNA and 12S rRNA, and nuclear histone H3 gene were amplified and sequenced as previously described [*Foltz et al.*, 2007; *Mah and Foltz*, 2011]. The obtained sequences of starfish were analyzed and compared with previous data from *Mah et al.* [2015]. The GenBank accession numbers for 16S rRNA, 12S rRNA, and H3 gene of starfish are KT258987, KT258986, and KT258988, respectively.

4. Plume Distributions

4.1. MAPR Surveys in 2011 on KR1 and KR2

Seven MAPR profiles on KR2 (Figure 1 and supporting information Table S1) found three sites, each separated by >25 km (Figure 1d; Stations 2, 16, and 14). Stations 2 and 16 each had multiple ΔNTU layers extending >300 m above bottom. ORP anomalies were robust at Station 2, indicating a nearby vent source,
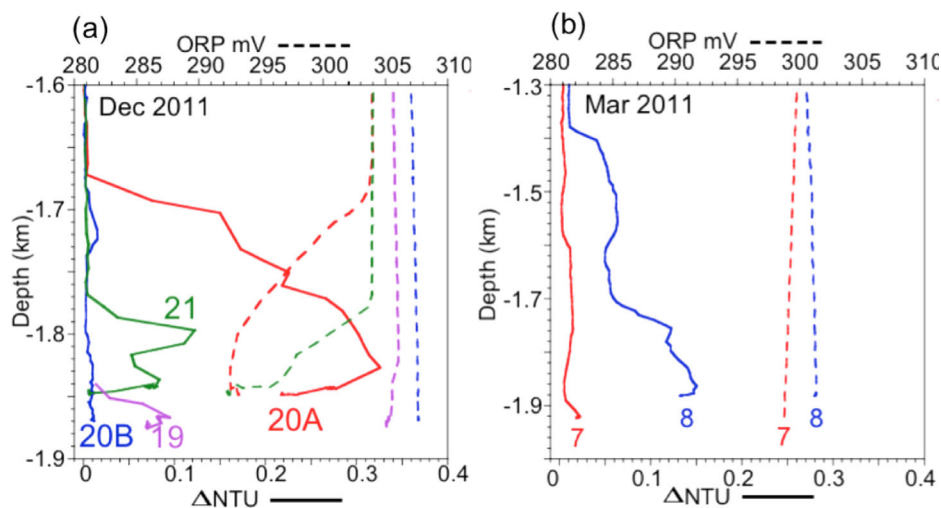
Figure 2. ΔNTU and ORP profiles of highly variable (a) and high rising (b) plumes, both implying short-lived hydrothermal events. At Station 20, cast A was conducted at 23:55 8 December; cast B at 15:17 10 December UTC. The anomalous ΔNTU at Station 20A between 1630 and 1670 m cannot be discerned at this scale. See section 4.1 for details.

and measureable at Station 16, indicating a vent source within ~1 km. No ORP anomaly was detectable at Station 14 (Figures 1b and 1d).

Forty MAPR profiles (Figure 1 and supporting information Table S1) were conducted along the KR1 axis during the March (8 profiles) and December (32 profiles) 2011 cruises, with a median separation distance of 6 km (range 1.7–30.6 km; Figures 1a and 1c). Seventeen profiles showed ΔNTU anomalies indicative of hydrothermal plumes, six of which also displayed distinct ORP anomalies. These profiles exclusively occurred on the two bathymetric highs of the supersegment. Fourteen occupied the relatively inflated, 125 km-long axial high section at the supersegment center, mostly on the shallowest subsegments, H2 and H3, adjacent to the intersection of the ridge axis by an off-axis seamount chain. Three other, apparently distinct, sites were found in segment P3 within the axial plateau area.

In two locations within segments H2 and H3, unique ΔNTU profiles indicate the possibility of short-lived hydrothermal events. In December, a single plume at Station 20 (Figure 1c; labeled 20A in Figure 2a) spanned 250 m from the seafloor to 1630 m, attaining a maximum ΔNTU of 0.33 at 1830 m, the highest ΔNTU value detected in any plume during all three cruises (Figure 2a). A high ORP anomaly throughout the entire plume indicated the plume-forming discharge was very recent (within days) and nearby. On-axis profiles conducted 1.5 h earlier and 3.5 km to the northeast (Station 19), and 2 h later and 6.1 km southwest (Station 21) found unusually high ΔNTU (>0.1) in near-bottom (>1780 m) plumes. However, a CTD profile conducted 40 h later at Station 20 (20B in Figure 2a) found only plumes of moderate ΔNTU and no ORP anomaly. Two plume characteristics at these three adjacent stations are consistent with a brief magmatic event. First, ΔNTU values >~0.1 are typical of plumes with a high concentration of particulate sulfur [*Baker et al.*, 1998; *Feely et al.*, 1999], primarily from abiotic precipitation of metal sulfides and bacterial manufacture of elemental sulfur. The latter is characteristic of increased bacterial biomass in the water column after seafloor eruptions [*Haymon et al.*, 1993; *Feely et al.*, 1999]. Second, a plume rise of 250 m through the local hydrography requires a point source heat flux ~10x higher than that for a 100 m rise [e.g., *Turner and Campbell*, 1987], a typical rise height for all other plumes observed elsewhere in December 2011.

In March, a multilayer plume at Station 8 (Figure 1c) reached to 1400 m (550 m above the seafloor) with a maximum ΔNTU of 0.16 (Figure 2b), a value exceeded during the entire study only by the Station 20 MAPR profile. Five kilometer away at Station 7, the maximum ΔNTU was only 0.018 but the plume top remained high, at ~1500 m. The Stations 7 and 8 plumes are thus additional evidence for occasional, but perhaps not rare, events of abnormally high hydrothermal discharge, as they require a 100-fold increase in point source heat flux relative to the normal rise of 100 m.

We can compare the spatial density of hydrothermal activity (plume incidence, p_h) along KR1 and KR2 to other intermediate-rate spreading ridges by calculating the fraction of MAPR casts detecting a plume
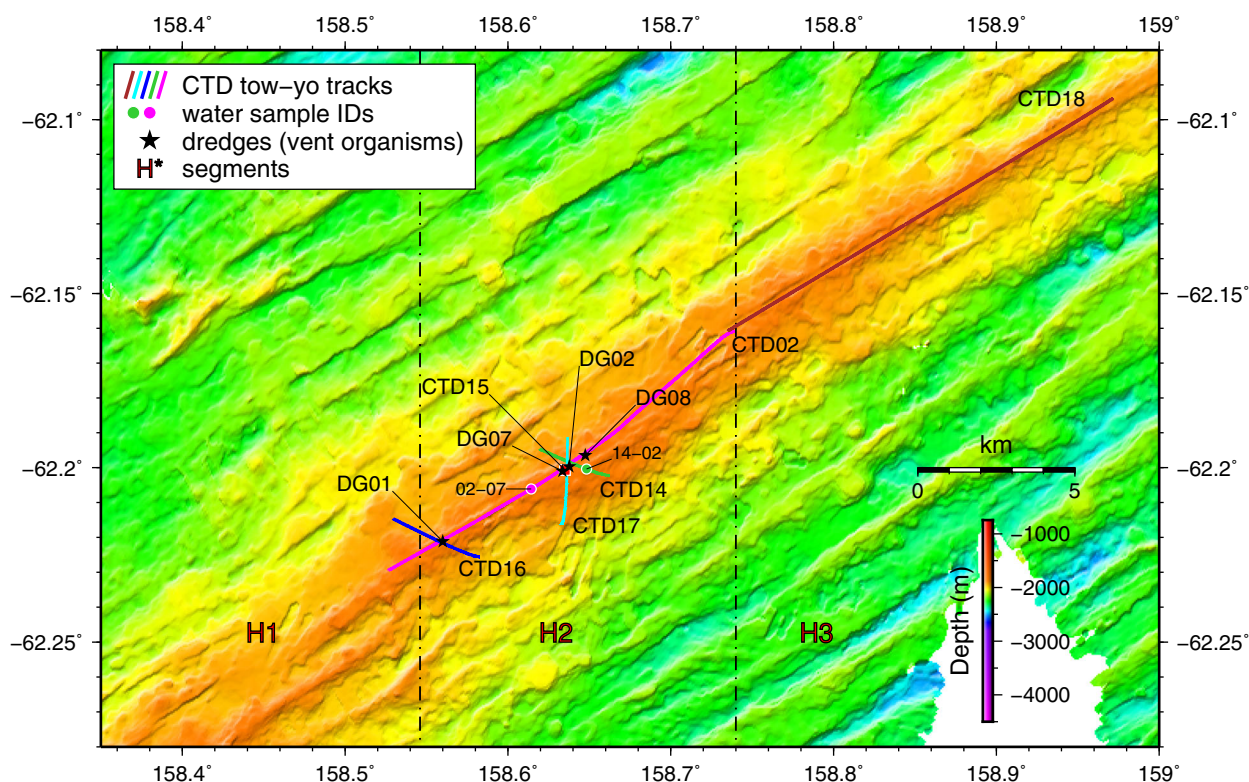
Figure 3. Hydrothermal plume and organism survey over Mujin vent field. CTD tow-yo and dredge locations are shown in colored lines and black stars, respectively. The vertical lines indicate boundaries of segments H1, H2, and H3. The green dot on CTD14 (sample 14-02) identifies a possible off-axis vent location (see also Figure 5).

[e.g., *Baker et al.*, 2014]. For this estimate, we do not consider results from the continuous plume survey by towed CTD along segments H2-H3 (discussed in section 4.2) as this high-resolution plume data would bias the results toward that plume-rich area. A simple calculation, based on 20 of 47 profiles detecting a plume, yields a $p_h = 0.43$. Calculations for KR1 and KR2 individually give the same value. Because the density of profiles varied among the morphological areas (0.05–0.18 profiles/km), a more appropriate calculation is the length-weighted mean p_h of all six morphological areas shown in Figures 1a and 1b (considering KR2 a single area). This approach gives $p_h = 0.34$ (with the p_h of individual areas ranging from 0 to 0.64), consistent with the prediction of 0.33 from the global trend of p_h for a spreading rate of ~ 70 mm/yr [*Baker et al.*, 2014]. This result agrees with that from a recent survey of hydrothermal plumes along the intermediate-rate (65–71 mm/yr) Southeast Indian Ridge from 77° to 100°E, where a MAPR plume survey found $p_h = 0.34$ (excluding anomalous segments on the Amsterdam-St. Paul hotspot plateau) [*Baker et al.*, 2014].

4.2. 2013 CTD Survey of Mujin Vent Field

In January–February of 2013, R/V *Araon* conducted CTD tow-yos and vertical casts on KR1 segments H1-H3 (Mujin vent field), plus two off-axis "background" stations. Tow-yos included CTDs 02 and 18, which together form a 28 km-long continuous along-axis transect from 158.5° to 159°E, and cross-axis tows CTD 14, 16, and 17, each ~3 km long (Figure 3). Peaks in the ΔNTU data indicate two areas with almost continuous hydrothermal plumes, centered near 158.6°E and 158.8°E, each extending ~ 6 km along axis (Figure 4). ORP anomalies identify two centers of venting in each area: 158.54°–158.57°E (M1) and 158.615°–158.642°E (M2) on H2, and 158.775°–158.8°E (M3) and 158.825°–158.851°E (M4) on H3.

The largest ORP decreases, at 158.64° and 158.78°E, both occur where the ΔNTU plumes come closest to the seafloor, likely marking discharge sites. Numerous other ORP anomalies within each venting area suggest multiple discharge sources arrayed along the axis. The most precise indicator of source location is the detection of a density inversion, signaling that the CTD passed through a still-rising buoyant plume. We observed five instances of rising plumes, four in M1 and M2 and a fifth in between but coincident with a sharp dE/dt decrease (Table 1, Figure 4 and supporting information Figure S1). Two occurred at an altitude
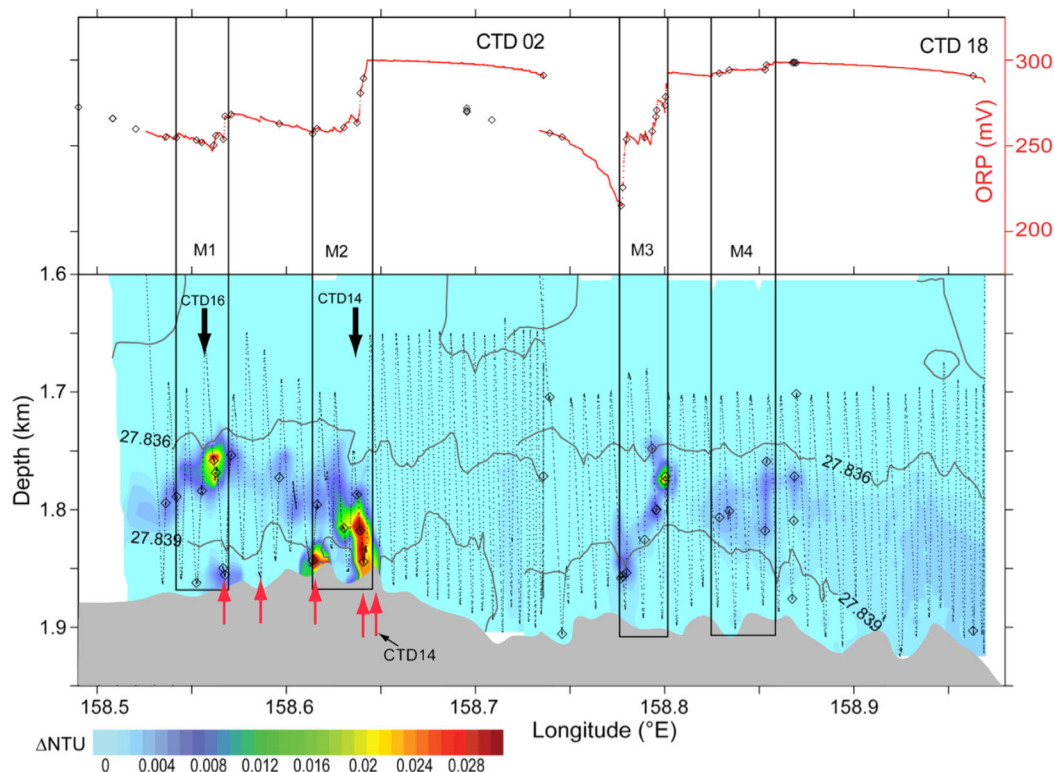
Figure 4. Along-axis plumes in segments H2 and H3 defined by ORP decreases and light-backscattering (ΔNTU) identify four major vent areas, M1–M4. Individual vent sites were precisely located by density inversions (red arrows; Table 1) where the CTD passed through a rising hydrothermal plume. Inversions were seen on CTD02 (not labeled) and CTD14. "CTD14" and "CTD16" mark the intersection with cross-axis tows shown in Figure 5. Both tows were conducted from east to west, and ORP anomalies are seen as sharp decreases followed by a slow recovery to non-plume values, which generally do not return to initial ORP values. However, ΔORP values are comparable throughout a tow, regardless of the initial ORP magnitude.

of ∼50 m on CTDs 02, 14, and one where a prominent plume extends upward from the seafloor (CTD02) and another at the CTD14 off-axis location (Figure 5). The remaining three, all close to the seafloor (≤ 25 m altitude), were detected on CTD02 at roughly 1 km intervals to the southwest along the axis. Thus even though active vents have not yet been imaged, the CTD data provide precise (±∼100 m, based on the uncertainty of the location of the CTD during tows) locations for several sites (Table 1 and Figure 4).

The cross-axis tows also provide insight about local plume dispersal (Figures 5a and 5b). All three tows showed plume dispersal solely to the north, suggestive of a current regime in which tidal fluctuations are incapable of broadening the plume footprints to extend south of the segment axis. Current fluctuations can also strongly influence plume rise height. For example, CTDs 14 and 17 crossed the axis at the same location ∼11 h apart, and the maximum observed plume rise height differed by ∼50 m. Nevertheless, plumes from both casts were capped by the 27.836 isopycnal, similar to plumes observed during CTDs 02 and 18 (Figure 4). Thus the vertical variability in that isopycnal explains why plume rise height can vary strongly among even closely spaced stations. The cross-axis tows also illustrate the improved location specificity of the ORP data, relative to the ΔNTU data. Decreases in ORP values occur within a few 100 m of the axis (except for the off-axis site detected on CTD14), whereas the ΔNTU plume extends well beyond the ORP anomalies.

Table 1. Characteristics of Five Density Inversions Encountered During CTD Tows in the Order From East to West

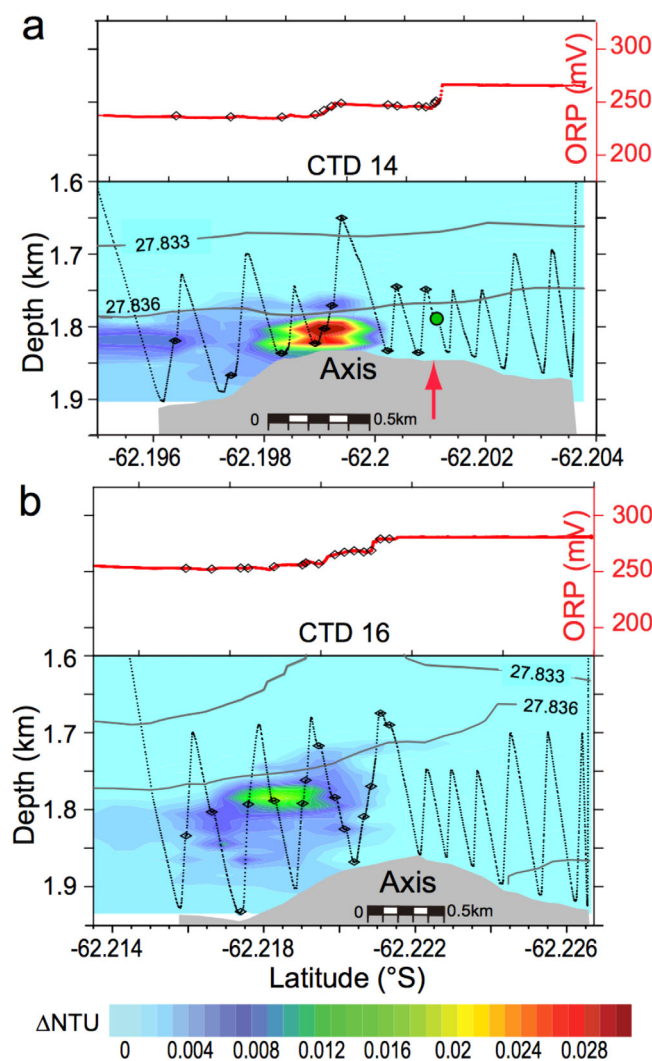| Cast	Longitude (°E)	Latitude (°S)	Depth (m)	Altitude (m)	$\Delta\sigma_\theta$	ΔNTU (V)	dE/dt (V/s)
CTD14	158.648	62.201	1803	50	0.0035	0.001	−0.90
CTD02	158.639	62.198	1815	50	0.0011	0.044	−0.5
CTD02	158.615	62.206	1842	25	0.0017	0.085	−0.11
CTD02	158.586	62.214	1856	20	0.0017	0.013	−0.23
CTD02	158.567	−62.219	1852	20	0.0023	0.023	−0.41

Figure 5. Plumes detected by cross-axis tows (a) CTD14 and (b) CTD16. In Figure 5a sample CTD14-02 is marked by a green dot on the towpath. A density inversion (red arrow) was observed at the same location. Both tows were conducted from south to north.

5. Plume Chemistry

5.1. Along-Axis Distribution of the Chemical Tracers

We collected water samples for the analysis of chemical tracers during tow-yos and vertical casts using the CTD-rosette system in 2013. CTD01 and CTD13 are background stations with neither substantial chemical enrichments nor NTU or ORP anomalies. The distribution of the chemical tracers, ORP, and NTU along the axis is shown in Figure 6 (supporting information Table S2).

Marked increases in ^{3}He, up to 3.8 fmol/kg, were observed in three general locations (M1–M3) within the Mujin vent field area (Figure 6a) with ^{3}He concentrations west of 158.5°E being close to background, suggesting that there are no significant hydrothermal sources at the western end of this segment. Aside from β-decay of tritium, responsible for the background δ^3He $(=[R_{sample}/R_{atm} - 1] \times 100\%,$ where R stands for ^{3}He/^{4}He in the sample or atmosphere; $R_{atm} = 1.384 \times 10^{-6}$) [Clarke et al., 1976] of ~9% near the ridge, chemically inert ^{3}He is sourced only from magmatic activity at deep ocean. Thus it is evident that samples collected in these areas with ^{3}He concentrations above background are hydrothermal plumes. This is also consistent with the pronounced anomalies of NTU and/or dE/dt found in these areas (Figures 6b and 6c).
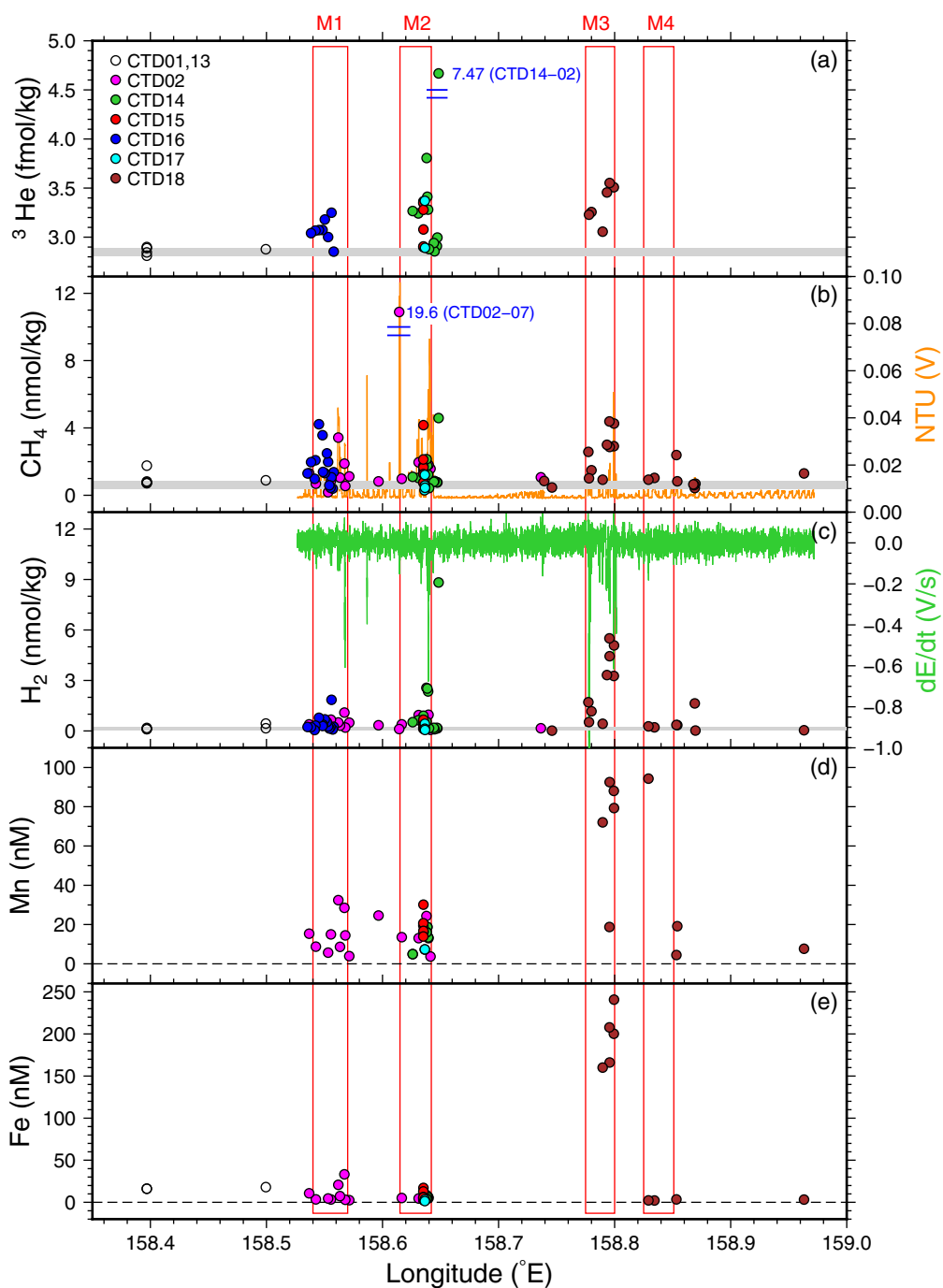
Additionally, a sample (CTD14-02; green circle in Figure 3) collected 500 m southeast of the ridge crest, with an exceptionally high value of ^{3}He = 7.47 fmol/kg, identified a slightly off-axis vent source. This sample also showed a strong ORP anomaly as well as a density inversion, but no significant ΔNTU.

The majority of the samples collected near the axis exhibited CH$_4$ concentrations above background (0.62 ± 0.23 nmol/kg), ranging from 1 to 5 nmol/kg. High concentrations were found near the vent areas (M1–M4) identified by elevated ^{3}He and ΔNTU and by lower dE/dt, suggesting a hydrothermal origin of methane. The highest concentration of 19.6 nmol/kg (CTD02-07; red circle in Figure 3) was found close to the bottom (within 24 m) at 158.615°E, where a density inversion was encountered during CTD02 (Table 1).

H$_2$ concentrations ranged between 0.04 and 8.8 nmol/kg, with a background concentration of 0.14 ± 0.09 nmol/kg (Figure 6c). More than 40 samples between 1750 and 1870 m exceeded 0.3 nmol/kg. The high values (3.3–5.5 nmol/kg) occurred around 158.8°E and were accompanied by strong dE/dt anomalies and elevated Mn and Fe concentrations. The highest value of 8.8 nmol/kg was measured at the off axis sample mentioned above (CTD14-02; 158.6483°E and 62.2004°S), which also had the highest ^{3}He (7.47 fmol/kg, or δ^3He = 131.8%), a strong ORP anomaly, but no ΔNTU (Figure 5b). Given the prevailing current to the north (Figure 5b) and no particle anomaly, this sample implies a vigorous low-temperature source south of the

Figure 6. Along-axis variation of chemical tracers. The background values (horizontal gray lines) of ^{3}He (2.85 ± 0.04 fmol/kg), CH$_4$ (0.62 ± 0.23 nmol/kg), and H$_2$ (0.14 ± 0.09 nmol/kg) are the mean and standard deviation of samples between 1600 and 1900 m at the background stations, CTDs 01 and 13. The background values of Mn and Fe (dotted lines) were chosen as zero because in many of the water samples measurable metal concentrations could not be detected. Along-axis variations in NTU (b) and dE/dt (c) are shown for comparison. The tracer concentrations around the vent areas (M1–M4) were substantially higher than the background values (the gray shades and dashed lines).

neovolcanic zone. The H$_2$ values in the Mujin field are typical for chronic hydrothermal plumes and much lower than observed in plumes above active eruptions [47–9123 nM, *Kelley et al.*, 1998; *Baker et al.*, 2011; *Resing et al.*, 2011].

Total dissolvable Mn (TDMn) and Fe (TDFe) were markedly enriched near the places with strong NTU and dE/dt anomalies. Both TDMn and TDFe concentrations were generally in the range of 0 (i.e., below detection

limit) to 40 nM (Figures 6d and 6e). Similar to H_2, the samples collected around 158.8°E showed substantially higher TDMn and TDFe concentrations than elsewhere, up to 94 and 241 nmol/L for TDMn and TDFe, respectively. The low values of TDMn and TDFe found at the off-axis site (CTD14-02) are consistent with the low ΔNTU value and an assumption of low-temperature venting.

5.2. Elemental Ratios of the Chemical Tracers

CH_4 can be examined in light of variations in the magmatic supply of ^{3}He, which allows sources of CH_4 to be more readily identified. Globally, $CH_4/^3$He ratios in MOR hydrothermal systems range between 0.1 and 300×10^6 [*Kawagucci et al.*, 2008 and references therein]. The highest values of $65–108 \times 10^6$ are often found at slow-spreading ridges (e.g., Rainbow, Lucky Strike, Menez Gwen [*Jean-Baptiste et al.*, 2004; *Charlou et al.*, 2000]), which is attributed to the production of abiogenic methane during serpentinization of ultramafic rock [*Charlou et al.*, 2002]. On the other hand, low values ($< 10 \times 10^6$) are linked to basaltic-hosted systems often found at fast spreading ridges such as the EPR [*Welhan and Craig*, 1983; *Merlivat et al.*, 1987; *Gharib et al.*, 2005]. $CH_4/^3$He ratios on KR1 mostly fell in the range of $1–5 \times 10^6$ (Figure 7b). However, slightly higher values of $7–17 \times 10^6$ were found in a group of samples collected $\sim$620 m northwest of the axis near 158.55°E during a cross-axis CTD tow-yo (CTD16; Figure 3). These samples exhibited modest ΔNTU, which correlated with a distinct enrichment in CH_4 ($\sim$4 nM). Because this is not an ultramafic system (MgO $<$ 8wt.%)[*Park et al.*, 2011], the enrichment in CH_4 may be associated with diffuse venting and biogenic carbon from either sediments within the off-axis vent fields (thermogenic) or from biological production (methanogenesis) in the subseafloor [*Kawagucci et al.*, 2013]. We disregard microbial oxidation of methane (methanotrophy) because it should reduce $CH_4/^3$He. Stable isotopes of CH_4 could be analyzed to discriminate these processes [*Proskurowski et al.*, 2008; *Kawagucci et al.*, 2008].

A majority of the samples exhibited $H_2/^3$He ratios $<3 \times 10^6$, but at M2 and M3 several samples are $>4 \times 10^6$. For example, around 158.8°E (M3) several samples displayed slightly higher $H_2/^3$He ($>5 \times 10^6$) consistent with elevated H_2, suggesting that the hydrothermal plumes here are younger than observed elsewhere [*Kelley et al.*, 1998]. Similarly, two samples at 158.64°E (M2) exhibited ratios $>4\times 10^6$. Those samples were collected over the axis during cross axis tow-yo CTD14. It is interesting to note that CTD14-02, boasting the highest ^{3}He and H_2 concentrations among the sample suite, has a modest $H_2/^3$He ratio of 1.9×10^6, typical of the majority of samples ($<3 \times 10^6$). This sample was collected in a buoyant plume (density inversion) so the plume was very young and a hydrothermal source was very close to CTD14-02. Therefore, the low $H_2/^3$He in this sample and perhaps for other samples cannot be attributed solely to a higher degree of microbial oxidation of H_2, assuming a constant oxidation rate in the KR1. The presence of two groups of samples ($H_2/^3$He $<3 \times 10^6$ and $H_2/^3$He $>4 \times 10^6$) suggests that the sources may have at least two different $H_2/^3$He ratios. Those samples with high $H_2/^3$He also exhibited distinctively higher H_2/CH_4 (>1; supporting information Figure S2). Additionally, given that the majority of samples exhibited relatively low H_2 and CH_4 (both <5 nmol/kg) and that H_2/CH_4 were in the range of 0.1–2.2, it is unlikely that there is significant organic source involved in H_2 enrichment [refer to Figure 6 of *Kawagucci et al.*, 2013]. If the H_2 observed here is produced from the reduction of water by reduced iron compounds in the rock [*Sansone et al.*, 1991; *McCollom and Seewald*, 2007], then the observed variability may be a result of age difference in the hydrothermal systems. That is, the system responsible for the majority of samples with lower ratios may come from older hydrothermal systems, which are more altered and thus produce less H_2 compared to that at 158.8°E [*Kelley et al.*, 1998]. However, there is no clear evidence that the higher $H_2/^3$He of $\sim$5 $\times 10^6$ at 158.8°E reflects a younger hydrothermal system and thus one that experienced a recent eruption. Instead, our plume data from 2011 suggest that M1 and M2 are areas where an event may have taken place, and those are areas that exhibit both lower H_2 and lower $H_2/^3$He. We note that values as low as 0.1×10^6 can be attributed to the microbial oxidation of H_2. In short, the KR1 ridge exhibits at least two distinctive $H_2/^3$He: (1) the one with the ratio $\sim$5 $\times 10^6$, responsible for the higher ratios at 158.8 and 158.64°E and, (2) the other with the ratio of $\sim$2 $\times 10^6$, applicable to the rest of samples, including CTD14-02.

Except for sample CTD02-07, the majority of samples along KR1 had relatively low CH_4/Mn, in the range of 0.03–0.5, which is similar to that observed elsewhere [*Gharib et al.*, 2005 and references therein]. Given that Mn has a greater than 2 week lifetime [*Kadko et al.*, 1990], the variation of CH_4/Mn is often ascribed to the processes resulting in the production or consumption of CH_4. For example, *Kawagucci et al.* [2008] observed a wide range of CH_4/Mn from 0.5 to 6 at Dodo Great Lava Plain (18°S) on the Central Indian Ridge and interpreted the variation as due to either CH_4 consumption by microbial methanotrophic activity or mixing among multiple hydrothermal plumes. A few samples around 158.8°E exhibited $CH_4/Mn < 0.01$ which can
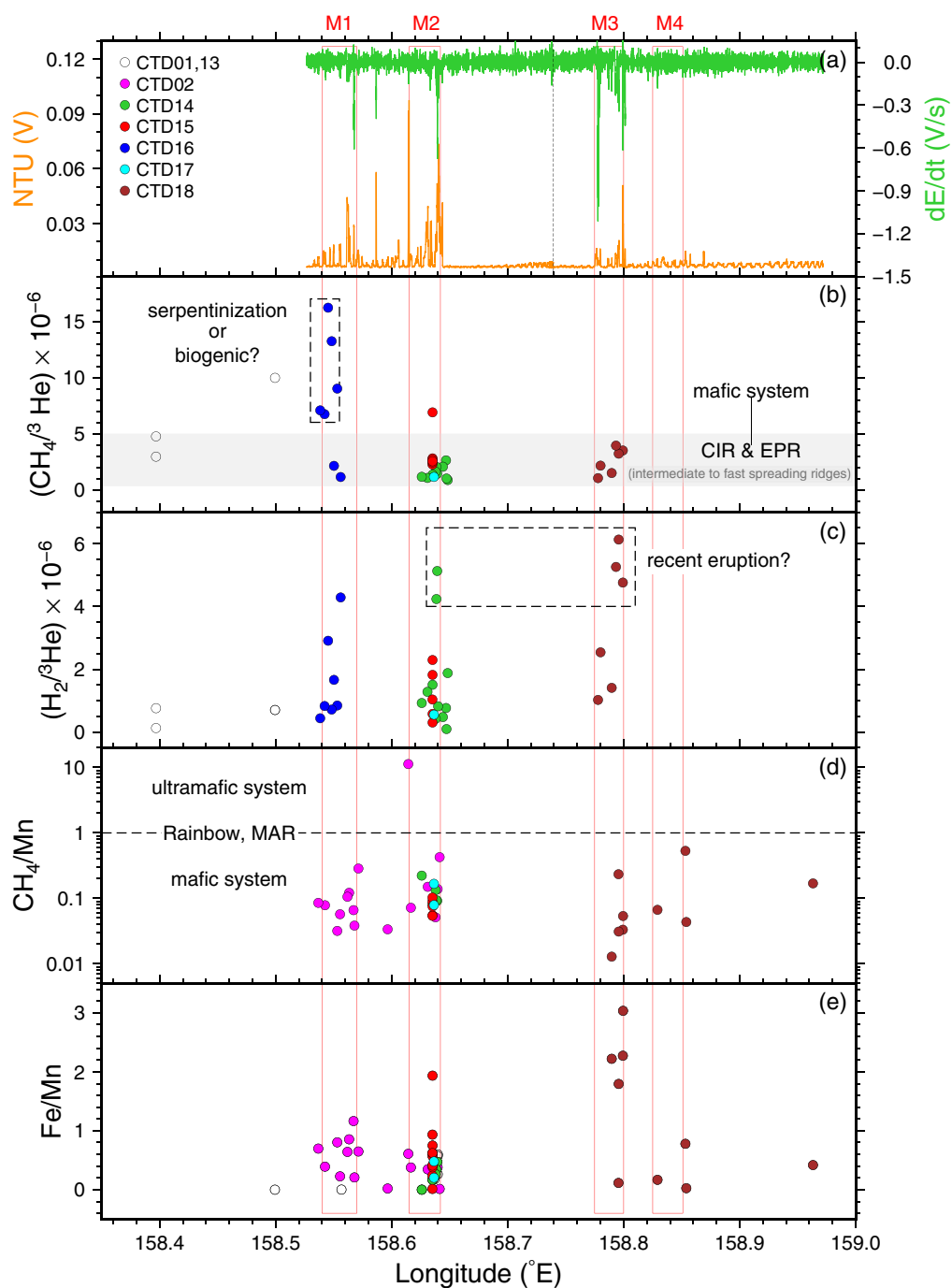
Figure 7. Along-axis variation of elemental ratios of the chemical tracers. The elemental ratios were calculated from the ratios between the background corrected tracer values. The overall ranges of $CH_4/^3He$ and CH_4/Mn suggest that the chemistry of Mujin vent field is akin to that of mafic-rock hosted system. The higher $H_2/^3He$ and Fe/Mn at M3 suggests that the plumes are originated from a system that experienced a recent eruption.

be attributed to the large excess of Mn. Overall, most of the ratios fell in the range of 0.01–0.5, which is typical for chronic plumes from a mafic rock-hosted system [*Lilley et al.*, 1995; *Ishibashi et al.*, 1997]. CTD02-07 had $CH_4/Mn = 11$ and corresponded to the highest CH_4 value along the ridge. These values have only been encountered in areas thought to be influenced by sedimentation [*Lilley et al.*, 1993], a recent eruption [*Mottl et al.*, 1995], or serpentinization of ultramafic rocks [e.g., Lucky Strike and Rainbow, *Charlou et al.*, 2000, 2002].

Figure 8. Photos of Kiwa crabs (Kiwa n. sp.) and a seven-armed Paulasterias starfish of the Mujin vent field of AAR.

The Fe/Mn ratios near M3 are >1 whereas those to the west at M1 and M2 are mostly <1. Fe/Mn between 1 and 7 is typical in high-temperature hydrothermal fluids [*Von Damm*, 1990] and plumes [e.g., *Baker et al.*, 2002] from MORs. Values <1 are generally found in lower temperature hydrothermal fluids and where H_2S is in excess of Fe [*Von Damm*, 1990; *Connelly et al.*, 2012], resulting in the removal of Fe as Fe-sulfides in both the subseafloor and during plume formation. Areas where $H_2S >$ Fe generally support abundant biological activity because sulfide is not bound to Fe [e.g., *Connelly et al.*, 2012] but the opposite is true when Fe $> H_2S$ and sulfide is mostly removed to Fe-sulfide phases. Two lines of evidence point to M1 and M2 being areas rich in hydrogen sulfide: high ΔNTU plumes observed in 2011, likely rich in elemental sulfur [e.g., *Baker et al.*, 2002], a primary oxidation product of H_2S; and low Fe/Mn ratios observed in 2013, suggestive of Fe removal as Fe sulfide.

6. Vent Organisms

Following the precise location of hydrothermal anomalies in the water column, rock dredges (Figure 3) recovered crabs and a seven-armed starfish that are associated with vent ecosystems (Figure 8). The crabs were identified as yeti crabs in the genus of *Kiwa*; molecular DNA sequences of mitochondrial 16S rRNA gene from two sampled yeti crabs showed 5.00%, 5.00%, and 5.80% genetic distances from those of *Kiwa hirsuta* of 38°S in the PAR and *Kiwa tyleri* of the ESR, and *Kiwa* n. sp. of SWIR, respectively. Because this degree of sequence divergence typically falls in a range of interspecific relationship, we consider the AAR yeti crab a potential new species of the genus *Kiwa*.

The crab specimens collected from Mujin also exhibit morphology that differs from southern ocean *Kiwa* species, such as *Kiwa tyleri* reported by *Thatje et al*. [2015] and *Kiwa* n. sp. SWIR reported by *Roterman et al.* [2013]. Compared to the smooth body surface of these two species, the potential new *Kiwa* species from the AAR has sparse setae on the body surface. This species has not been found previously in the western Pacific near the AAR despite intensive surveys. The genus has been found in cold seeps in the continental margin off Costa Rica [*Thurber et al.*, 2011], on the northeast PAR [*MacPherson et al.*, 2005], the SWIR [*Roterman et al.*, 2013], and the ESR [*Rogers et al.*, 2012], and thus appear to be widely distributed in the southern oceans.

The seven-armed starfish collected from Mujin exhibits similar morphology to the vent associated starfish, *Paulasterias tyleri*, of the ESR reported by *Mah et al.* [2015] in that it has seven arms and dense spinelets on the aboral and lateral surface. Furthermore, the 16S rRNA, 12S rRNA and H3 gene sequences showed 99.5%, 99.6% and 100% identity, respectively, to those of *P. tyleri*, suggesting that they may be the same species distributed across vent habitats of the Southern Ocean. Detailed description of the two species will be published elsewhere.

The presence of *Kiwa* species on the AAR raises the possibility that all CAR might be biogeographically connected. Although these chemosynthetic vent sites are distant from one another, ancestors of *Kiwa* crabs must have colonized them through evolutionary dispersals along the past and present ridge axes.

The seven-armed *Paulasterias* starfish on the AAR is also evidence for a close and strong evolutionary connectivity between vent fields in the southern ocean because of the morphological and close genetic similarities of the Mujin specimens with *Paulasterias tyleri* found at ESR vent fields and at a Southern Ocean site near the Ross Sea [see Figure 1 and Table 1 of *Mah et al.*, 2015]. The Circum-Antarctic current might aid the hemispheric biological connectivity of southern ocean ridges, but testing this hypothesis awaits intensive biological sampling.

7. Conclusions

Hydrothermal plumes along KR1 and KR2, two previously uncharted segments of the AAR, were mapped with 47 MAPR profiles. These data demonstrate that the spatial density of hydrothermal activity along KR1 and KR2 ($p_h = 0.34$) is consistent with the prediction of 0.33 from the global trend for a spreading rate of 68 mm/yr [*Baker et al.*, 2014]. The densest site concentration on KR1 occurred along a relatively inflated, 20 km-long section near the segment center, which we refer to as the Mujin (Misty Harbor) hydrothermal field. The $CH_4/^3He$ (1–15 $\times$ 10^6) and CH_4/Mn (0.01–0.5) ratios of water samples are consistent with basaltic-hosted vent systems. Overall, the plume density and chemistry of KR1 are similar to that found on other intermediate-rate spreading ridges. However, we also note that plume characteristics can vary on smaller temporal and spatial scales. The high rising (>550 m) plume near M1 and M2 found in 2011 implies an event that generated a point source heat flux a 100-fold higher than that of the $\sim$100 m-rise plumes elsewhere on the ridge. In 2013, an unusually high number of buoyant, rising plumes encountered during our survey indicates either the presence of many individual vent sources along M1 and M2 or an abundance of disorganized high-temperature flow similar to that observed after eruptions on the northern EPR [*Von Damm et al.*, 1995]. This is consistent with extremely high particle ($\Delta NTU > 0.1$) loads in 2011, which are likely produced by abundant sulfur [*Feely et al.*, 1999] and ongoing eruptive activity [*Baker et al.*, 2011]. In this same area in 2013, low Fe levels, combined with particle-rich plumes, moderately elevated Mn, and low Fe/Mn indicate robust hydrothermal venting with excess H_2S available to nurture chemosynthetic biota at the seafloor. The Mujin field was also populated by *Kiwa* crabs and seven-armed *Paulasterias* starfish. The presence of these crabs and starfish raises the possibility that all Southern Ocean ridges and deep seas might be biogeographically connected. More intensive biological sampling on the circum-Antarctic Ridges will be required to test this hypothesis.

References

American Public Health Association (1985), *Standard Methods for the Examination of Water and Wastewater*, 16th ed., 1268 pp., Am. Publ. Health Assoc., Washington, D. C.

Baker, E. T., G. J. Massoth, R. A. Feely, G. A. Cannon, and R. E. Thomson (1998), The rise and fall of the Coaxial hydrothermal site, 1993–1996, *J. Geophys. Res*, 103(B5), 9791–9806, doi:10.1029/97JB03112.

Baker, E. T., et al. (2002), Hydrothermal venting along Earth's fastest spreading center: East Pacific Rise, 27.5°–32.3°, *J. Geophys. Res.*, 107(B), 2130, doi:10.1029/2001JB000651.

Baker, E. T., F. Martinez, J. Resing, S. Walker, N. J. Buck, and M. H. Edwards (2010), Hydrothermal cooling along the Eastern Lau Spreading Center: No evidence for discharge beyond the neovolcanic zone, *Geochem. Geophys. Geosyst.*, 11, Q08004, doi:10.1029/2010GC003106.

Baker, E. T., J. E. Lupton, J. A. Resing, T. Baumberger, M. D. Lilley, S. L. Walker, and K. H. Rubin (2011), Unique event plumes from a 2008 eruption on the Northeast Lau Spreading Center, *Geochem. Geophys. Geosyst.*, 12, Q0AF02, doi:10.1029/2011GC003725.

Baker, E. T., C. Hémond, A. Briais, M. Maia, D. S. Scheirer, S. L. Walker, T. Wang, and Y. J. Chen (2014), Correlated patterns in hydrothermal plume distribution and apparent magmatic budget along 2500 km of the Southeast Indian, *Geochem. Geophys. Geosyst.*, 15, 3198–3211, doi:10.1002/2014GC005344.

Beaulieu, S., E. T. Baker, C. R. German, and A. Maffei, (2013), An authoritative global database for active submarine hydrothermal vent fields, *Geochem. Geophys. Geosyst.*, 14, 4892–4905, doi:10.1002/2013GC004998.

Charlou, J. L., J. P. Donval, E. Douville, and P. Jean-Baptiste (2000), Compared geochemical signatures and the evolution of Menez Gwen (37°50′N) and Lucky Strike (37°17′N) hydrothermal fluids, south of the Azores Triple Junction on the Mid-Atlantic Ridge, *Chem. Geol.*, 171, 49–75.

Charlou, J. L., J. P. Donval, Y. Fouquet, and P. Jean-Baptiste (2002), Geochemistry of high H2 and CH4 vent fluids issuing from ultramafic rocks at the Rainbow hydrothermal field (36°14′N, MAR), *Chem. Geol.*, 191, 345–359.

Choi, H., S. Kim, and S. Park (2013), Interpretation of bathymetric and magnetic data from the easternmost segment of Australian-Antarctic Ridge, 156°–161°E, Abstract # T13A-2498 presented at AGU, Fall Meeting 2013, AGU, San Francisco, Calif.

Clarke, W. B., W. J. Jenkins, and Z. Top (1976), Determination of tritium by mass spectrometric measurement of ³He, *Int. J. Appl. Radiat. Isot.*, 27, 515–522.

Connelly, D. P., et al. (2012), Hydrothermal vent fields and chemosynthetic biota on the world's deepest seafloor spreading centre, *Nat. Commun.*, 3, 620, doi:10.1038/ncomms1636.

Corliss, J. B., et al. (1979), Submarine thermal sprirngs on the galapagos rift. *Science, 203*, 1073–1083.

Feely, R. A., E. T. Baker, G. T. Lebon, J. F. Gendron, J. A. Resing, and J. P. Cowen (1999), Evidence for iron and sulfur enrichments in hydro-thermal plumes at Axial Volcano following the January–February 1998 eruption, *Geophys. Res. Lett.*, *26*(24), 3649–3652, doi:10.1029/1999GL002325.

Foltz, D., M. Bolton, S. Kelley, B. Kelley, B., and A. Nguyen (2007), Combined mitochondrial and nuclear sequences support the monophyly of forciculatacean sea stars, *Mol. Phylogenet. Evol.*, *43*(2), 627–634.

German, C. R., and W. E. Seyfried Jr. (2014), Hydrothermal processes, in *Treatise on Geochemistry*, edited by H. D Holland and K. K. Turekian, pp. 191–233, Elsevier, Oxford, U. K., doi:10.1016/B978-0-625 08-095975-7.00607-0.

German, C. R., et al. (2008), Hydrothermal activity on the southern Mid-Atlantic Ridge: Tectonically- and volcanically-controlled venting at 4-5°degrees S, *Earth Planet. Sci. Lett.*, *273*, 332–344.

Gharib, J. J., F. J. Sansone, J. A. Resing, E. T. Baker, J. E. Lupton, and G. J. Massoth (2005), Methane dynamics in hydrothermal plumes over a superfast spreading center: East Pacific Rise, 27.5°–32.3°S, *J. Geophys. Res.*, *110*, B10101, doi:10.1029/2004JB003531.

Haymon, R. M., et al. (1993), Volcanic eruption of the mid-ocean ridge along the East Pacific Rise crest at 9°45–52′N: Direct submersible observations of seafloor phenomena associated with an eruption event in April, 1991, *Earth. Planet. Sci. Lett.*, *119*, 85–101.

Ishibashi, J., H. Wakita, K. Okamura, E. Nakayama, R. A. Feely, G. T. Lebon, E. T. Baker, and K. Marumo (1997), Hydrothermal methane and manganese variation in the plume over the superfast-spreading southern East Pacific Rise, *Geochim. Cosmochim. Acta*, *61*(3), 485–500.

Jean-Baptiste, P., E. Fourré, and J. L. Charlou (2004), Helium isotopes at the Rainbow hydrothermal site (Mid-Atlantic Ridge, 36°14′N), *Earth Planet. Sci. Lett.*, *221*, 325–335.

Jordan, A., and B. Steinberg (2011), Calibration of atmospheric hydrogen measurements, atmospheric measurement techniques, *Atmos. Meas. Tech.*, *4*, 509–521.

Kadko, D. C., N. D. Rosenberg, J. E. Lupton, R. W. Collier, and M. D. Lilley (1990), Chemical reaction rates and entrainment within the Endeav-our Ridge hydrothermal plume, *Earth Planet. Sci. Lett.*, *99*(4), 315–335.

Kawagucci, S., K. Okamura, K. Kiyota, U. Tsunogai, Y. Sano, K. Tamaki, and T. Gamo (2008), Methane, manganese, and helium-3 in newly dis-covered hydrothermal plumes over the Central Indian Ridge, 18°–20°S, *Geochem. Geophys. Geosyt.*, *9*, Q10002, doi:10.1029/2008GC002082.

Kawagucci, S.,Y. Ueno, K. Takai, T. Toki, M. Ito, et al. (2013), Geochemical origin of hydrothermal fluid methane in sediment-associated fields and its relevance to the geographical distribution of whole hydrothermal circulation, *Chem. Geol.*, *339*, 213–225, doi:10.1016/j.chemgeo.2012.05.003.

Kelley, D., M. Lilley, and J. Lupton (1998), Enriched H$_2$, CH$_4$, and ^{3}He concentrations in hydrothermal plumes associated with the 1996 Gorda Ridge eruptive event, *Deep Sea Res., Part 2*, *45*, 2665–2682.

Lilley M. D., D. A. Butterfield, E. J. Olson, J. E. Lupton, S. A. Macko, and McDuff R. E. (1993) Anomalous CH, and NH: Concentrations at an unsedimented mid-ocean-ridge hydrothermal system, *Nature*, *364*, 45–47.

Lilley, M. D., R. A. Feely, and J. H. Trefry (1995), Chemical and Biochemical Transformations in Hydrothermal Plumes, in *Seafloor Hydrothermal Sys-tems: Physical, Chemical, Biological, and Geological Interactions*, edited by S. E. Humphris, et al., pp. 369–391, AGU, Washington, D. C.

Lupton, J., and L. Evans (2013), Changes in the atmospheric helium isotope ratio over the past 40 years, *Geophys. Res. Lett.*, *40*, 6271–6275, doi:10.1002/2013GL057681.

Lupton, J. E. (1990), Water column hydrothermal plumes on the Juan de Fuca Ridge, *J. Geophys. Res.*, *95*(B8), 12,829–12,842, doi:10.1029/JB095iB08p12829.

Macpherson, E., W. Jones, and M. Segonzac (2005), A new squat lobster family of Galatheoidea (Crustacea, Decapoda: Anomura) from the hydrothermal vents of the Pacific-Antarctic Ridge, *Zoosystema*, *27*(4), 709–723.

Mah, C., and D. Foltz (2011), Molecular phylogeny of the Forcipulatacea (Asteroidea: Echinodermata): Systematics and biogeography. *Zool. J. Linn. Soc.*, *162*(3), 646–660.

Mah, C., K. Linse, J. Copley, L. Marsh, A. Rogers, D. Clague, D., and D. Foltz (2015), Description of a new family, new genus, and two new spe-cies of deep-sea Forcipulatacea (Asteroidea), including the first known sea star from hydrothermal vent habitats. *Zool. J. Linn. Soc.*, *174*(1), 93–113.

McCollom, T. M., and J. S. Seewald (2007), Abiotic synthesis of organic compounds in deep-sea hydrothermal environments, *Chem. Rev.*, *107*(2), 382–401.

Measures, C. I., J. Yuan, and J. A. Resing (1995), Determination of iron in seawater by flow injection analysis using in-line preconcentration and spectrophotometric detection, *Mar. Chem.*, *50*, 3–12.

Merlivat, L., F. Pineau, and M. Javoy (1987), Hydrothermal vent waters at 13°N on the East Pacific Rise: Isotopic composition and gas con-centration, *Earth Planet. Sci. Lett.*, *84*, 100–108.

Mottl, M. J., F. J. Sansone, C. G. Wheat, J. A. Resing, E. Baker, and J. E. Lupton (1995), Hydrothermal plumes along the East Pacific Rise, 8°40′ to 11o50′N: Dissolved manganese and methane, *Geochim. Cosmochim. Acta. 59*, 4147–4165.

Park, S. H., C. H. Langmuir, J. Lin, D. Hahm, S. S. Kim, S. G. Hong, Y. M. Lee, and P. Michael (2011), Preliminary results of a recent expedition to the Australian-Antarctic Ridge [Goldschmidt abstracts], *Mineral. Mag.*, *75*(3), 1600.

Proskurowski, G., M. D. Lilley, and E. J. Olson (2008), Stable isotopic evidence in support of active microbial methane cycling in low-temper-ature diffuse flow vents at 9°50′N East Pacific Rise, *GEOCHIMICA ET COSMOCHIMICA ACTA*, *72*(8), 2005–2023, doi:10.1016/j.gca.2008.01.025.

Resing, J. A., and M. J. Mottl (1992), Determination of manganese in seawater using flow injection analysis with on-line preconcentration and spectrophotometric detection, *Anal. Chem.*, *64*(22), 2682–2687.

Resing, J. A., et al. (2011), Active submarine eruption of boninite in the northeastern Lau Basin, *Nat. Geosci.*, *4*(11), 799–806.

Reynolds, J. R., C. H. Langmuir, J. F. Bender, K. A. Kastens, and W. B. F. Ryan (1992), Spatial and temporal variability in the geochemistry of basalts from the East Pacific Rise, *Nature*, *359*, 493–499.

Rhee, T. S. (2000), The process of air-water gas exchange and its application, PhD thesis, Tex. A&M Univ., College Station.

Rhee, T. S., A. J. Kettle, and M. O. Andreae (2009), Methane and nitrous oxide emissions from the ocean: A reassessment using basin-wide observations in the Atlantic, *J. Geophys. Res.*, *114*, D12304, doi:10.1029/2008JD011662.

Rogers, A. D., et al. (2012), The discovery of new deep-sea hydrothermal vent communities in the Southern Ocean and implications for biogeography, *PLoS Biol.*, *10*(1), e1001234, doi:10.1371/journal.pbio.1001234.

Roterman, C. N., J. T. Copley, K. T. Linse, P. A. Tyler, and A. D. Rogers (2013), The biogeography of the yeti crabs (Kiwaidae) with notes on the phylogeny of the Chirostyloidea (Decapoda: Anomura), *Proc. R. Soc. B*, 280, 1–9, doi:10.1098/rspb.2013.0718.

Sansone, F. J., J. A. Resing, G. W. Tribble, P. N. Sedwick, K. M. Kelly, and K. Hon (1991), Lava-seawater interactions at shallow-water submar-ine lava flows, *Geophys. Res. Lett.*, *18*(9), 1731–1734, doi:10.1029/91GL01279.

Stoffers, P., T. Worthington, R. Hekinian, S. Petersen, M. Hannington, and M. Türkay (2002), Silicic volcanism and hydrothermal activity documented at Pacific-Antarctic Ridge. *Eos Trans. AGU*, *83*(28), 301–304.

Tamura, K., G. Stecher, D. Peterson, A. Filipski, and S. Kumar (2013). MEGA6: Molecular evolutionary genetics analysis version 6.0. *Mol. Biol. Evol.*, *30*, 2725–2729.

Tao, C., et al. (2007), First discovery and investigation of a high-temperature hydrothermal vent field on the ultra- slow spreading Southwest Indian Ridge, *Eos Trans. AGU*, *88*(52), Fall Meet. Suppl., Abstract T52B-07.

Thatje, S., L. Marsh, N. Roterman, M. Mavrogordato, and K. Linse (2015), Adaptations to hydrothermal vent life in Kiwa tyleri, a new species of yeti crab from the East Scotia Ridge, Antarctica. *PLoS One*, *10*(6), e0127621, doi:10.1371/journal. pone.0127621.

Thurber, A. R., W. J. Jones, and K. Schnabel (2011), Dancing for food in the deep sea: Bacterial farming by a new species of Yeti Crab, *PLoS One*, *6*(11), e26243, doi:10.1371/journal.pone.0026243.

Turner, J. S., and I. H. Campbell (1987), Temperature, density and buoyancy fluxes in black smoker plumes, and the criterion for buoyancy reversal, *Earth Planet. Sci. Lett.*, *86*, 85–92.

Von Damm, K. L. (1990), Seafloor hydrothermal activity black smoker chemistry and chimneys, *Annu. Rev. Earth Planet. Sci.*, *18*, 173–204.

Von Damm, K. L., S. E. Oosting, R. Kozlowski, L. G. Buttermore, D. C. Colodner, H. N. Edmonds, J. M. Edmond, and J. M. Grebmeier (1995), Evolution of East Pacific Rise hydrothermal vent fluids following a volcanic eruption, *Nature*, *375*, 47–50.

Van Dover, C. L., C. R. German, K. G. Speer, L. M. Parson, and R. C. Vrijenhoek (2002), Evolution and biodiversity of deep-sea vent and seep invertebrates, *Science*, *295*, 1253–1257.

Van Dover, C. (2000), *The Ecology of Deep-Sea Hydrothermal Vents*, Princeton Univ. Press, N. J.

Walker, S. L., E. T. Baker, J. A. Resing, K. Nakamura, and P. D. McLain (2007), A new tool for detecting hydrothermal plumes: An ORP sensor for the PMEL MAPR [abs.], *Eos Trans. AGU*, *88*(52), Fall Meet. Suppl., Abstract V21D-0753.

Welhan, J. A., and H. Craig (1983), Methane, hydrogen and helium in hydrothermal fluids at 21°N on the East Pacific rise, in Hydrothermal Processes at Seafloor Spreading Centers, NATO Conference Series. 12, edited by P.A Rona et al, pp. 391–409, Springer, N. Y.

Young, C., and J. E. Lupton (1983), An ultratight fluid sampling system using cold-welded copper tubing, *EOS Trans. AGU*, *64*, 735.